Assessment and application of tomographic PIV for the spray-induced flow in an IC engine

Assessment and application of tomographic PIV for the spray-induced flow in an IC engine

B. Peterson[1], E. Baum[2], C.-P. Ding[2], D. Michaelis[3], A. Dreizler[2], B. Böhm[4]

[1]Institute for Energy Systems, Department of Mechanical Engineering, School of Engineering, University of Edinburgh, The King's Buildings, Mayfield Road, Edinburgh, EH9 3JL, UK

[2]Fachgebiet Reaktive Strömungen und Messtechnik (RSM), Technische Universität Darmstadt, Jovanka-Bontschits-Straße 2, 64287 Darmstadt, Germany

[3]LaVision GmbH, Anna-Vandenhoeck-Ring 19, 37081 Göttingen, Germany

[4]Fachgebiet Energie- und Kraftwerkstechnik (EKT), Technische Universität Darmstadt, Jovanka-Bontschits-Straße 2, 64287 Darmstadt, Germany

Corresponding author: Brian Peterson, The King's Buildings, Mayfield Road, Edinburgh, EH9 3JL, Scotland, UK, Fax: +44 (0)131 650 6554, E-mail: brian.peterson@ed.ac.uk

Colloquium: Engine

Paper length

- Main text (Introduction to Acknowledgements): 3693
- Equations: 0
- Nomenclature: N/A
- References: (25+2)x2.3x7.6=472
- Tables:
  - Tab. 1: (6+2)x7.6+3=64
- Figures & figure captions:
  - Fig. 1: (57+10)x2.2x1+2=149
  - Fig. 2: (46+10)x2.2x1+13=136
  - Fig. 3: (53+10)x2.2x2+11=288
  - Fig. 4: (46+10)x2.2x1+5=128
  - Fig. 5: (35+10)x2.2x2+15=213
  - Fig. 6: (105+10)x2.2x2+26=532
  - Fig. 7: (51+10)x2.2x1+15=149
  - Fig. 8: (71+10)x2.2x2+18=374
  - Total figures: 1969
- Reference + table + Figures = 2505

Total count: 6198 < 6200

Abstract

Spray-induced turbulence proceeding late-injection is regarded to augment mixing, playing a primary role in controlling heat-release rates and pollutant formation in direct-injection engines. This work presents the first application of tomographic PIV (TPIV) to resolve the 3-dimensional, 3-component (3D3C) spray-induced turbulent flow in a spray-guided direct-injection spark-ignition (SG-DISI) engine. TPIV measurements were performed after a single-injection from a hollow-cone spray when particle distributions were suited for accurate particle reconstruction. High-speed PIV (HS-PIV) measurements (4.8kHz) were combined with phase-locked TPIV measurements (3.3Hz) to provide the time history of the 2D2C flow-field preceding TPIV. HS-PIV is also used to validate TPIV measurements within the z=0mm plane. TPIV uncertainties of 12% are assessed for non-injection operation. TPIV is used to spatially resolve spray-induced turbulent kinetic energy (TKE), shear (S), and vorticity (Ω) distributions. The added 3D3C velocity information is capable of resolving 3D shear layers that produce spatially-coherent 3D turbulent vortical structures, which are anticipated to augment fuel-air mixing. Measurements spatially quantify the increase of these parameters from injection and quantity distributions reveal significant differences to non-injection operation. The isosurface density ($\bar{\rho}$), defined as the volume percentage for which a flow parameter exceeds a given value, identified distributions of the largest TKE, S, and Ω magnitudes, which indicated the highest turbulence levels. Distributions quantify the increase of TKE, S, and Ω from injection and describe the decay of spray-induced turbulence with time. At $\bar{\rho}$ values below 10%, fuel injection increases TKE, S, and Ω magnitudes in excess of 400% compared to the tumble flow without injection. Magnitudes remained 2-times larger than non-injection operation 16 crank-angle degrees (CADs) after injection, indicating that spray-induced turbulence enhancement can remain for a significant time after injection. Measurements and analyses provide insight into spray-induced turbulence phenomena and are anticipated to support predictive model development for engine sprays.

Keywords: tomographic particle image velocimetry (TPIV), planar particle image velocimetry, spray-induced turbulent flow, IC engine

Assessment and application of tomographic PIV for the spray-induced flow in an IC engine

B. Peterson, E. Baum, C.-P. Ding, D. Michaelis, A. Dreizler, B. Böhm

1. Introduction

The in-cylinder turbulent flow plays a pivotal role in mixture preparation, combustion, and pollutant formation in direct-injection (DI) engines [1]. Injection of liquid fuel in excess of 10MPa during compression can enhance or disturb the pre-existing flow-field. For swirling engine flows, fuel injection has shown to redistribute and strengthen the angular momentum in the piston bowl, providing repeatable swirl-flow patterns [2] and enhancing fuel-air mixing for improved combustion [1]. However, the spray often greatly disturbs the tumbling flow, modifying the large-scale central axis-of-rotation and inducing higher turbulence levels. This spray-induced tumble flow experiences greater cycle-to-cycle variations (CCV) in flow structure, which can lead to improper fuel-air transport [3-4] and increased rate of combustion instabilities in spark-ignition (SI) engines [5-6].

Within the engine/spray community there is a need to better understand the spray-induced turbulent flow to ensure proper mixing, transport, and combustion stability within DISI engines. Therefore, researchers have focused on fundamentals of liquid-gas momentum exchange [7], spray-induced mixing and thermal transport [8-10], spray/flow interactions focusing on CCV [3-5], and the physics of spray-induced turbulence [11-15]. The latter is important because it is suggested that late-mixing, flame speed, and heat-release rate for stratified operation is not determined by intake generated turbulence, but rather by the turbulence generated from injection [15].

Laser-based diagnostic measurements and engine-spray simulations have provided our current understanding of spray-induced flow physics. Experimentally, particle image velocimetry (PIV) has provided a majority of flow/spray knowledge [2-8,11,16,17]. While planar-PIV has provided a powerful understanding of flow/spray physics, the limitations of 2D data inhibit the understanding of an inherently 3D phenomenon. Instantaneous 3D3C flow-fields are required to fully resolve the spray-induced shear-layers that produce spatially-coherent turbulent vortical flow structures for enhanced mixing and flame-front transport. Such measurements are also

highly sought to develop predictive models for optimizing flow patterns, mixing, and improving injector/engine compatibility. Holographic PIV has captured 3D spray velocities [18], but limited to sparse particle fields. Tomographic PIV (TPIV) and tomographic particle tracking velocimetry have been applied within engines to capture the complexity of the 3D flow motion and resolve the complete velocity gradient tensor [19-23]. TPIV should principally be suited for engine-spray environments if locally dense particle distributions can be managed.

This paper presents the first application of TPIV to resolve the 3D3C spray-induced flow within a SG-DISI optical engine. TPIV measurements are obtained after injection when particle distributions are suitable for accurate TPIV particle reconstruction. Planar high-speed PIV (HS-PIV) measurements (4.8kHz) are combined with TPIV (3.3Hz) to provide a time-history of the fuel-spray and 2D2C flow-field preceding the phase-locked, single-cycle TPIV measurements. HS-PIV also provides TPIV validation within the central symmetry plane (z=0mm). TPIV is further used to investigate the 3D turbulent kinetic energy (TKE) and the complete shear (S) and vorticity (Ω) tensors. Measurements spatially quantify the increase in TKE, S, and Ω from injection and describe how the spray-induced turbulence disperses within the FOV and decays with time due to molecular diffusion and dissipation.

2. Experimental

Velocimetry measurements were performed in a 4-stroke single-cylinder SG-DISI optical engine operating at 800RPM. Operating conditions are shown in Table 1. The engine is equipped with a 4-valve pent-roof cylinder head, centrally-mounted injector, centrally-mounted spark plug, and quartz-glass cylinder and flat piston. Further details of the engine are described in [20,24]. Silicone oil droplets (1µm diameter) were seeded into the intake air for PIV, but fuel droplets also influence velocimetry measurements. Isooctane was injected through a centrally-mounted, outwards opening piezo-actuated injector (105^{o} spray angle) within 18MPa injection pressure. The injector operated with 400µs injection duration and end-of-injection (EOI) of 76^{o} before top-dead-center (bTDC). The amount of fuel injected was 2.9mg/cycle. This injection event mimics the first-injection typically utilized amongst a multi-injection strategy [3-4]. The resulting in-cylinder flow after injection is important because it implicates flow stability and proper fuel-air transport for subsequent injections [3-4]. Injection timing utilized here occurs earlier than typical DISI stratified-charge operation. The

injection timing was chosen to maintain suitable particle distributions for TPIV processing (0.02-0.08 particles/pixel) and allow for ~15 crank-angle degrees (CADs) to study the evolution of the spray-induced flow. After 60°bTDC, TPIV image quality suffered due to scattered light from the cylinder head and approaching piston. Consequently, TPIV images were not acquired after 60°bTDC.

Table 1:
Engine operating conditions

Engine speed	800RPM
Intake press. / temp.	0.95bar / 300K
Fuel (C_8H_{18}) / EOI	2.9mg/cycle / 76°bTDC
Inj. Press. / Temp.	18MPa / 333K
Intake Press. / Temp	95kPa / 295K
Charge density at EOI	2.0 kg/m^3

Figure 1 shows the experimental setup for the combined TPIV and planar HS-PIV. A dual-cavity frequency-doubled Nd:YAG (Spectra Physics, 350mJ/pulse, 3.3Hz) was used for TPIV. The laser beam passed through a half-wave plate (p-polarized) and two cylindrical lenses to expand and collimate laser light to specify the laser sheet thickness (5mm). The light passed through a polarizing beam-splitter and another set of cylindrical lenses to expand and collimate the beam to specify the laser sheet width. Laser light was reflected off a 45° mirror in the crankcase, providing a vertically illuminated volume in the engine. Four interline transfer sCMOS cameras (LaVision), with identical 100mm lenses (Tokina) in Scheimpflug arrangement were arranged circularly around the engine. TPIV camera angles were modified from [19] to provide the maximum range of camera angles suitable for the field-of-view (FOV). Wider angles between cameras 3,4 also accommodated the HS-PIV camera. Each camera projection provided an independent line-of-sight information of the illuminated volume (50x*H*x5mm^3; height (*H*) determined by piston position) centered within the cylinder axis.

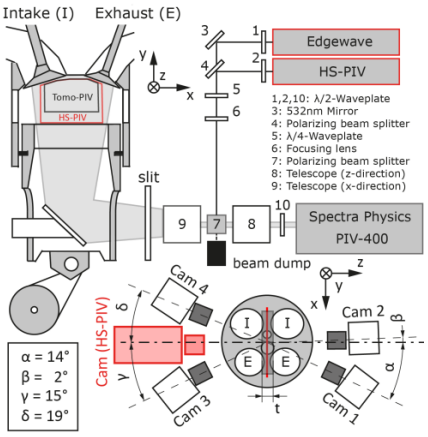

Fig. 1: Experimental Setup

A second dual-cavity, frequency-doubled Nd:YAG laser (Edgewave, 8mJ/pulse, 4.8kHz) was used for planar HS-PIV. The laser beam passed through a quarter-wave plate (circularly polarized) and a set of focusing optics before being combined with the TPIV laser at the polarizing beam-splitter. Only the s-polarized light of the HS-PIV laser (~50% of energy, i.e. 4mJ/pulse) was reflected and used for experiments. After the polarizer, the HS-PIV laser light passed through the same focusing optics as the TPIV system. The HS-PIV laser sheet of 1mm thickness was positioned within the center plane of the TPIV volume (i.e. z=0mm). A CMOS camera (Phantom V.711) was placed between TPIV cameras 3,4 and imaged onto a 55xHmm^2 FOV.

Camera and laser systems were synchronized to the engine at 800RPM. HS-PIV images were recorded at crank-angle resolution from 85^{o}bTDC until the CAD before TPIV was acquired, providing the 2D2C flow-field evolution before TPIV. This was performed for TPIV images acquired at 70^o and 60^{o}bTDC. HS-PIV images were not acquired after TPIV because of the sCMOS long second exposure time (20ms); any additional light source (e.g. HS-PIV laser or combustion) within the second TPIV exposure negatively biased TPIV measurements. The laser pulse separations (DT) were $DT_{HS\text{-}PIV}$=12µs and DT_{TPIV}=15µs to resolve the spray-induced flow-field. HS-PIV images were acquired for 288 consecutive cycles, while TPIV images were recorded every 2nd cycle to acquire 300 phase-locked images at 70^o and 60^o bTDC. Limited disk space of the HS-PIV camera (8GB) prevented the camera from recording more than 288 cycles. This limited the number of synchronized HS-PIV/TPIV sequences.

Additional phase-locked TPIV images were taken from 74°-69°bTDC (100 cycles each CAD). HS-PIV was not performed for this sequence. These 100-image TPIV datasets were recorded to study the 3D3C spray-induced flow evolution after EOI. Particle distributions were too dense to utilize TPIV before 74°bTDC. TPIV datasets from 68°-61°bTDC were performed with a 2nd fuel injection, which is not presented in this work for brevity. TPIV datasets from 68°-61°bTDC with single-injection were not performed. The TPIV dataset at 60°bTDC with single-injection is used to describe relevant trends as CAD progresses past 69°bTDC.

TPIV and HS-PIV were processed with DaVis 8.2.1 (LaVision). Images of a spatially defined target (LaVision) within the engine were used to calibrate images and match viewing planes of each camera system. A 15 pixel sliding minimum subtraction and local intensity normalization were applied during TPIV image pre-processing. A volume self-calibration was performed for 100 images without injection. This provided a remaining pixel disparity <0.2 pixels. 3D particle reconstruction was performed using an iterative Multiplication Algebraic Reconstruction Technique algorithm (FastMART). TPIV was calculated by direct volume correlation with decreasing volume size (final size: 64x64x64 pixels) with 75% overlap, providing a 1.5x1.5x1.5mm^3 spatial resolution (based on the final interrogation window size) and 0.375mm vector spacing in each direction. HS-PIV images were cross-correlated with decreasing window size, multi-pass iterations from 64x64 to 32x32 pixels with 75% overlap, providing a 3.0x3.0x1.0mm^3 spatial resolution and 0.75mm vector spacing in the *x*-*y* direction.

3. TPIV assessment and HS-PIV

Mass conservation is applied to ascertain TPIV uncertainty. This is applied for non-injection operation when density is considered spatially uniform. Continuity yields: $\rho^{-1}(\partial\rho/\partial t) + \partial u_i/\partial x_i = 0$ and is assessed at 70°bTDC. Here, $\partial u_i/\partial x_i \approx 10^4 s^{-1}$, while the term $\rho^{-1}(\partial\rho/\partial t) = 85 s^{-1}$ is less significant and will be ignored. Continuity is assessed similar to [19] for cubic control volumes (CV) of equidistant grid-spacing (0.375mm) throughout the entire measurement volume for 300 images. In attempt to quantify the relative deviation from mass conservation, the velocity difference ($\Delta U = \Delta u + \Delta v + \Delta w$) is normalized with the average velocity $\left(|V|_{3D,CV}\right)$ that enters each CV. The PDF of $\Delta U/|V|_{3D,CV}$ is shown in Fig. 2 (top/right axes). The $\Delta U/|V|_{3D,CV}$ distribution is symmetric around zero. The standard deviation (σ=12%) represents the

deviation of the velocity flux and is reported as the TPIV uncertainty. For reference, the $\Delta U/|V|_{3D,CV}$ PDF for injection is also shown in Fig. 2, but this distribution cannot be used to ascertain mass conservation because density is spatially variant and not quantified.

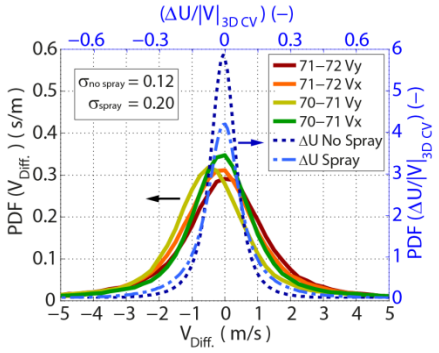

Fig. 2: PDF of $\Delta U/|V|_{3D,CV}$ (dash-lines, right/top axis) and HS-PIV/TPIV velocity differences (solid-lines, left/bottom axis).

HS-PIV measurements were used to assess TPIV for fuel injection. Figure 3 presents the evolution of the spray-induced flow-field captured by HS-PIV (78°-71°bTDC) and TPIV (70°bTDC) and provides a qualitative comparison between HS-PIV and TPIV. The top row shows Mie scattering images from an individual cycle at selected CADs, while the bottom row shows the corresponding 2D2C velocity field (z=0mm) represented by streamlines. The TPIV Mie scattering image is taken from camera 2, which viewed nearly perpendicular to the imaging volume. Mie images in Fig. 3 are normalized by the maximum intensity for better visual representation since HS-PIV/TPIV images were acquired with different light sources.

At 78°bTDC liquid spray regions are masked, but the remaining flow-field shows an upward entrainment motion and the preceding clockwise tumble motion. After injection, the tumble motion does not exist in the FOV. The spray-induced flow exhibits velocities exceeding 16m/s with two counter-rotating vortices on the left and an upward entrainment-like flow exists to the right. The counter-rotating vortices are a result of the toroidal vortex formed in the shear layers inside and outside of the expired hollow-cone spray [3]. As time progresses, the counter-rotating vortices separate and velocity magnitude decreases, while the upward entrainment-like flow remains with $|V|_{2D}$=10m/s.

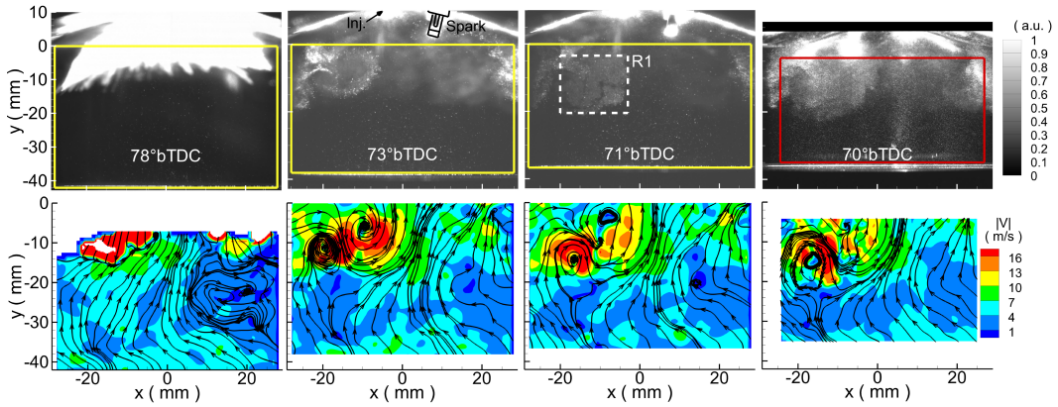

Fig. 3: Image sequence for instantaneous spray cycle. HS-PIV 78°-71°bTDC, TPIV (z=0mm) 70°bTDC.

The HS-PIV x- and y-velocity components (71°bTDC) at each point in space are subtracted from TPIV velocity components (70°bTDC) to assess the differences in HS-PIV and TPIV images. For reference, this difference is also performed for HS-PIV between 72° and 71°bTDC. Differences are evaluated within the z=0mm TPIV domain at the HS-PIV resolution. Figure 2 shows PDFs of these velocity differences (bottom/left axis). Velocity differences are not expected to exactly equal zero because data is extracted at different CADs and velocity changes with CAD. PDFs for 71°-72° and 70°-71°bTDC show similar distributions, demonstrating that HS-PIV and TPIV are in agreement. Findings indicate that TPIV is as reliable as the HS-PIV measurements and validates TPIV for the engine-spray environment within this study.

Fuel droplets, acting as tracer particles, influence velocimetry findings. In order to not disturb gas-flow measurements, fuel droplets should behave similarly to silicone oil droplets and accurately follow the gas-flow. A PTV algorithm (LaVision) was applied to the HS-PIV dataset to identify individual fuel and oil droplets of diameter (d) and intensity (I) within region R1 (see Fig. 3) for injection and non-injection operation (288 cycles). Non-injection findings identified oil droplets (average diameter: $\overline{d_{oil}} = 1\mu m$) with an average intensity of $\overline{I_{oil}} = 650$ counts. Individual droplet diameters for injection operation were estimated by: $d_{droplet} = \overline{d_{oil}} \times \sqrt{I_{droplet}/\overline{I_{oil}}}$. Maximum droplet intensities (3318 counts) were below the camera saturation level. The fuel droplet response time is calculated as: $t_o = \rho_{fuel} {d_{fuel}}^2 / 18\mu_{air}$, where $\rho_{fuel} = 690 kg/m^3$ and $\mu_{air} = 2.30e^{-5} Ns/m^2$ (evaluated for $T_{air} = 400K$ [25]). Response time increases by 20% if μ_{air} is evaluated at 300K. Figure 4 shows t_o vs. $d_{droplet}$ evaluated in R1 at 74°bTDC and 71°bTDC (for

clarity). Particle response times range from $t_o = 1.8 - 9.9\mu s$, corresponding to $d_{droplet} = 0.9 - 2.5\mu m$ (fuel or oil). $d_{droplet}$ and t_o decrease with CAD via secondary breakup and evaporation. Response times remain below 10μs (i.e. >100 kHz frequency response), indicating that fuel droplets accurately follow the gas-flow and do not disturb velocimetry measurements. This is not unexpected since images occur 0.6-3.3ms after injection in an expired spray plume.

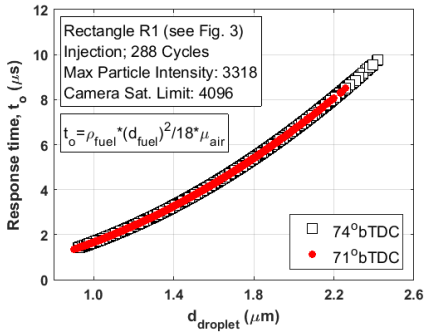

Fig. 4: Droplet response time vs. diameter.

4. TPIV Results and Discussions

TPIV is applied to spatially resolve the spray-induced 3D-TKE and instantaneous S and Ω distributions. Measurements spatially quantify the increase in TKE, S, and Ω from injection and distributions are compared against non-injection operation. Analysis describes how the turbulent-infused fuel-cloud spatially evolves within the FOV and statistically reveals the turbulence decay with time due to molecular diffusion and dissipation [12-14]. Quantifying spray-induced turbulence at the CADs presented is important to understand (1) rapid fuel-air mixing for proper fuel preparation and emission reduction, (2) spray-flow behavior that impacts fuel delivery for proceeding injections, (3) flame front transport for very early spark timings, and (4) development of predictive models that accurately describe these phenomena.

4.1 3D Turbulent Kinetic Energy (TKE)

Turbulence is first assessed by 3D-TKE defined as: $TKE = \frac{1}{2}\left(\overline{u_i' u_i'}\right)$, where u_i' is the fluctuating velocity component in the *i*th direction. TKE is calculated by Reynolds decomposition (100 cycles). Figure 5 shows isosurfaces of 3D-TKE at selected CADs after injection. The ensemble-average velocity, shown in the *z*=0mm plane, reveals the evolution of the spray-induced counter-rotating vortices and upwards entrainment velocity.

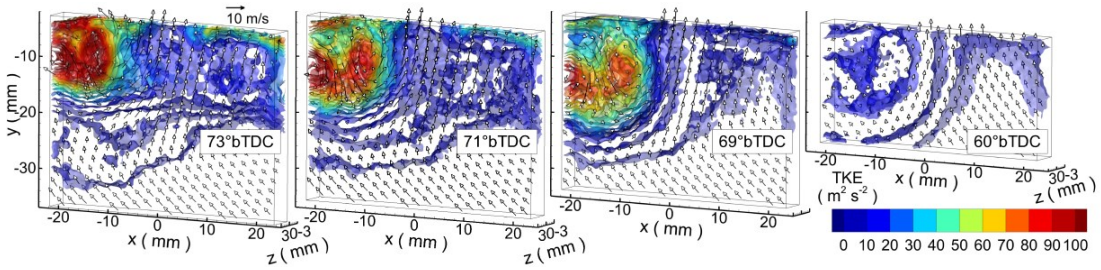

Fig. 5: 3D-TKE isosurfaces and ensemble-average velocity (100 cycles, every 29th vector shown, z=0mm) at select CADs.

TKE and average velocity magnitude are largest within the fuel-cloud with TKE≥100m^2/s^2 and $|\bar{V}|_{3D}$≥15m/s. As time progresses from 73º-69ºbTDC, the fuel-cloud and entrainment vortices progress into the FOV, while maximum TKE and velocity magnitudes reduce. Highest TKE values are located near the center of the counter-rotating vortices and TKE magnitudes decrease radially. Along the cylinder axis (x=0mm), the strong upward entrainment-like flow ($|\bar{V}|_{3D}$=10m/s) with relatively low TKE values (<20m^2/s^2) remains from 73º-69ºbTDC. At 60ºbTDC, TKE values from the injection have reduced significantly (<20m^2/s^2) and the upward entrainment velocities are largest in the FOV (~5m/s). TKE values outside of the fuel-cloud (e.g. lower-right in FOV) remain below 10m^2/s^2 for all CADs, representing similar magnitudes as non-injection operation (see Fig. 8).

The computed TKE fields are associated with turbulence levels and fluctuations of large-scale coherent flow structures (i.e. CCV) [21]. Individual TPIV images (not shown) indicate that both high turbulence levels and CCV contribute to the high TKE values in the spray region. The strong upward entrainment flow however, is more repeatable, exhibiting lower TKE values for the operating conditions.

A 300-image dataset exists at 70ºbTDC. Comparison between 100- and 300-image datasets (see supplemental material) revealed similar velocity and TKE distribution; local differences were less than 5% on average. Strong agreement between datasets argues that the 100-image datasets adequately capture the relevant TKE findings presented.

4.2 Instantaneous shear and vorticity distributions

Analysis of the complete shear (S) and vorticity (Ω) tensors for CADs 74º-69º and 60ºbTDC are further used to study instantaneous spray-induced turbulence. Unlike TKE, assessment of S and Ω does not require

Reynolds decomposition; thus they are not directly biased by CCV. Access to the complete S and Ω tensors enable quantitative measurements of spatially coherent 3D vortical flows produced from the 3D spray-induced shear layers. These aspects emphasize the advantage of instantaneous 3D3C measurements to characterize the in-cylinder turbulence.

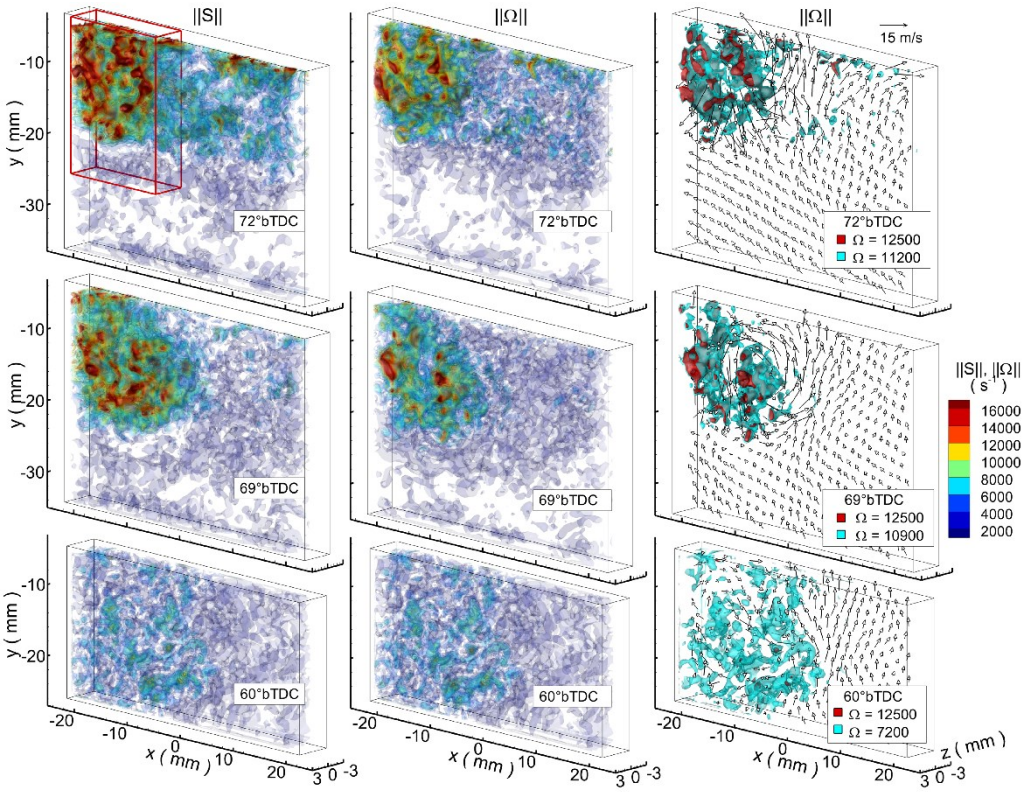

Fig. 6: 3D isosurfaces of instantaneous ||S|| (left), ||Ω|| (middle), and threshold-based ||Ω|| with 3C velocity field (z=0mm, every 21st vector shown) (right). Each CAD represents different cycles.

Figure 6 presents a sequence of single-cycle images at selected CADs to illustrate the progression of instantaneous spray-induced S and Ω within the FOV. Each CAD represents a different cycle. The Frobenius norm (||…||) represents shear and vorticity magnitudes, which are evaluated within the remaining discussion. 3D ||S|| and ||Ω|| isosurfaces are shown in the left and middle columns, while the 3C velocity (z=0mm) and threshold-based ||Ω|| isosurfaces (based on average isosurface density, $\bar{\rho}_{\Omega}$ (see Fig. 8)) are shown in the right column. Isosurface density is defined as the percentage of voxels exceeding a threshold (V_{thresh}) to total number of voxels (V_{total}) [21]. This identifies the distribution of largest Ω-magnitudes occupying a percentage of the volume domain. ||Ω|| thresholds shown represent $\bar{\rho}_{\Omega,74bTDC}$=4% (||Ω||≥12500s^{-1}, red) and $\bar{\rho}_{\Omega,CAD}$=4%

(blue) to demonstrate the declination of largest 4% Ω-magnitudes at CAD nearest to EOI (i.e. 74°bTDC), while visualizing the distribution of largest Ω-magnitudes occupying 4% volume for subsequent CADs. Figure 7 presents PDFs of ||S||,||Ω|| in the "spray-zone" (red-rectangle, Fig. 6) to quantify distributions for 100 cycles and complement the analysis presented in the single-cycle sequence.

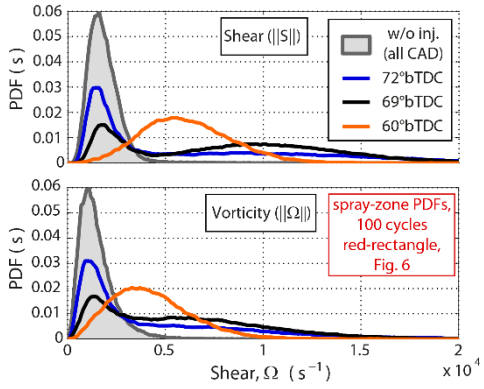

Figure 7: ||S||,||Ω|| PDFs of "spray-zone" at selected CADs. Non-injection PDFs represented at same CADs as injection.

In Fig. 6, the fuel-cloud is represented where ||S||,||Ω||≥8000s^{-1}. Largest ||S||,||Ω|| exceeding 1.6x10^{4}s^{-1} exist as individual cylindrically/spherically shaped pockets. At fixed CADs, ||S|| distributions exhibit larger magnitudes than ||Ω|| (see also ||S||,||Ω|| PDFs, Fig. 7) and pockets of large ||Ω|| intermittently appear in the periphery of large shear regions. This reveals that the spray-induced flow is primarily shear driven, producing intermittent coherent turbulent structures (i.e. entrainment vortices) containing large ||Ω||.

As CAD progresses from 72°-69°bTDC, the fuel-cloud progresses further into the FOV, while pockets of high ||S||,||Ω|| decrease in size and magnitude. A spray-induced roll-up vortex forms along the periphery of high shear-layers. PDFs, shown in Fig. 7, exhibit a more pronounced bimodal distribution at 69°bTDC with less occurrence of ||S||,||Ω||<2000s^{-1} as the fuel-cloud moves further into the FOV. Fast-forwarding to 60°bTDC, regions of ||S||,||Ω||≥8000s^{-1} have dissipated and remaining regions of large ||S||,||Ω|| have moved further into the FOV. A clockwise-rotating vortex remains the flow remnant in the dissipated fuel-cloud, while the upward entrainment flow remains to the right. At 60°bTDC, locations with ||Ω||≥12500s^{-1} are reduced to spherical pockets representing <0.5% of the total volume. The 60°bTDC PDFs in Fig. 7 exhibit Gaussian-like distributions centered near the bimodal inflection point at 69°bTDC.

For reference, non-injection PDFs at the same CADs are shown in Fig. 7 to illustrate the spray-induced ||S||,||Ω|| enhancement. PDFs without injection do not change for 74-60°bTDC. At 72°bTDC, regions within the red-rectangle, but outside the fuel-cloud, mimic non-injection distributions. PDFs deviate further from non-injection distributions at 69°bTDC. PDFs at 60°bTDC indicate that distributions tend back toward non-injection distributions, but demonstrate that spray-induced ||S||,||Ω|| remain larger than the non-injection flow well after EOI.

4.3 Decay of spray-induced turbulence using $\bar{\rho}$ distributions

Figure 8a-c describes the evolution of spray-induced TKE, S, and Ω distributions for all imaged CADs. Figure 8a-c shows 0-10% $\bar{\rho}$ distributions vs. threshold for TKE, ||S||, and ||Ω|| (100 cycles). This describes the distributions of highest magnitude for each variable (indicating highest turbulence levels) to quantify the evolution of spray-induced turbulence with CAD. All $\bar{\rho}$ curves exhibit a decaying trend with CAD, indicating a decrease in parameter magnitude and turbulence level with CAD. Curves show a consistent decrease with CAD from 74°-72°bTDC. From 72°-70°bTDC, TKE continues to decrease with CAD, while ||S|| and ||Ω|| curves only show minimal decrease. As illustrated in Fig. 6, the turbulent-infused fuel-cloud progresses within the FOV, encompassing a larger volume, but ||S||,||Ω|| decrease in magnitude. The rate at which high-valued spray-induced ||S||,||Ω|| quantities progress within the volume domain appears to balance the rate at which ||S||,||Ω|| reduce in magnitude. After 70°bTDC $\bar{\rho}$-distributions continue decreasing and show a large decrease as CAD jumps from 69°-60°bTDC. Although CAD data from 68°-61°bTDC is unavailable, the decreasing trend is clear and captures the decay of TKE, ||S||, and ||Ω|| with CAD.

Figure 8a-c also shows TKE, ||S||, and ||Ω|| for non-injection operation at the same CADs, revealing the enhancement of such parameters from injection. For the $1 \leq \bar{\rho} \leq 5\%$ range, spray-induced TKE magnitudes are >400% larger than non-injection operation (74°-69°bTDC), while ||S||,||Ω|| are up to 350% larger than non-injection operation. At 60°bTDC, spray-induced quantities are reduced, but values remain twice those of non-injection operation, revealing the turbulence enhancement remains 16 CAD after EOI.

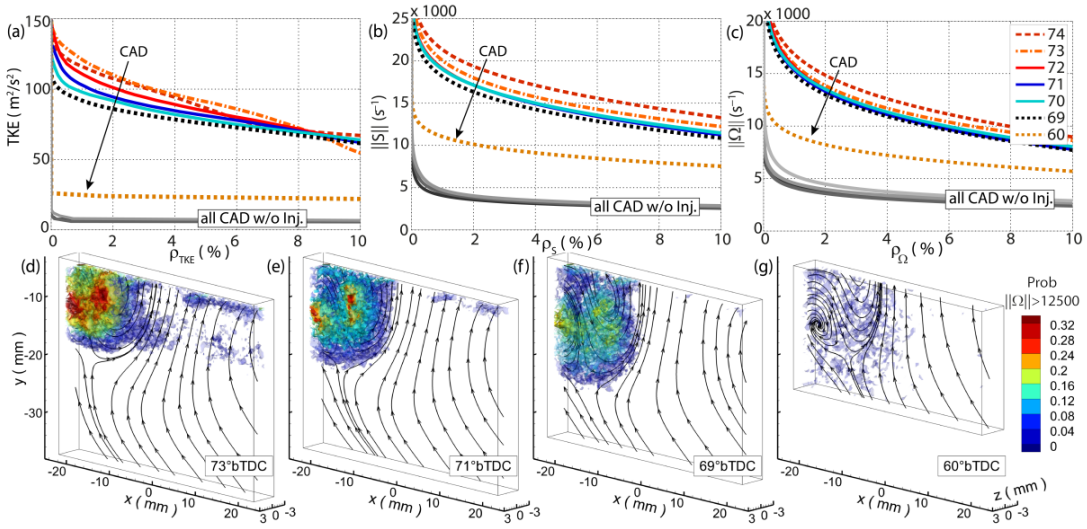

Figure 8: (a-c) Average TKE, ||S||, and ||Ω|| isosurface density with CAD, (d-g) probability isosurfaces for $||\Omega|| \geq 12500 s^{-1}$ at selected CADs.

Figure 8d-g shows the spatially resolved decay of ||Ω|| with CAD in the volume domain. 3D isosurfaces corresponding to the probability that the local flow exceeds $||\Omega||=12500 s^{-1}$ are shown at selected CADs. This Ω-threshold represents the largest Ω occupying 4% volume at 74°bTDC (i.e. Ω-threshold at $\bar{\rho}_{\Omega,74bTDC}$=4%). The image sequence shows the most-probable locations of large ||Ω|| and the reduced tendency of high vorticity occurring as CAD progresses. The ensemble-average flow is represented by streamlines. Probabilities exceeding 20% exist in the center of the fuel-cloud region and decrease radially and with CAD. Highest probabilities (>30%) occur near the center of the counter-rotating vortices, identifying locations of highest turbulence. At 60°bTDC, turbulence levels have decreased and the probability of $||\Omega|| \geq 12500 s^{-1}$ falls below 4%. However, without injection, flows at 60°bTDC did not exhibit $||\Omega|| \geq 12500 s^{-1}$ values, further revealing the turbulence enhancement from injection well after EOI.

Conclusions

Spray-induced turbulence proceeding late-injection augments mixing, thus playing a primary role in controlling heat-release rates and pollutant formation. TPIV was applied to resolve the 3D3C spray-induced flow within a SG-DISI optical engine. TPIV measurements were obtained after a single-injection from a hollow-cone spray when particle densities were suited for accurate particle reconstruction. This injection mimics the first-injection from a multi-injection strategy. HS-PIV measurements (4.8kHz) were combined

with TPIV (3.3Hz) to provide the time-history of the 2D2C flow-field preceding TPIV images. TPIV uncertainties were assessed (12%) and measurements were validated with HS-PIV (z=0mm plane).

TPIV was used to spatially resolve 3D-TKE and ||S||,||Ω|| distributions, otherwise not available with planar PIV. Measurements spatially quantify the increase of these parameters from injection and distributions are compared against non-injection operation. Analysis revealed the progression of the turbulent-infused fuel-cloud within the FOV and quantified the turbulence decay with CAD after EOI. For the engine operation, parameter magnitudes increased as high as 400% from injection and remained 2-times larger than non-injection operation 16 CADs after EOI, indicating that spray-induced turbulent enhancement remains for a significant time-period after injection. Measurements and analyses provide insight into spray-induced turbulence phenomena and are appropriate to support predictive model development for engine sprays. Measurements beyond 60ºbTDC or for fired-operation were not performed, but are envisioned for future experiments. Higher temperatures are expected at these conditions such that spray-induced turbulence may exhibit a faster decay than shown here. Later injection and imaging timings will provide assessment of spray-induced turbulence for enhanced flame-front transport.

Acknowledgements

Financial support by DFG (PE 2068 and Gottfried Wilhelm Leibniz program) and SFB/TRR 150 are gratefully acknowledged. The authors are especially grateful to LaVision for equipment loan.

Supplemental Data

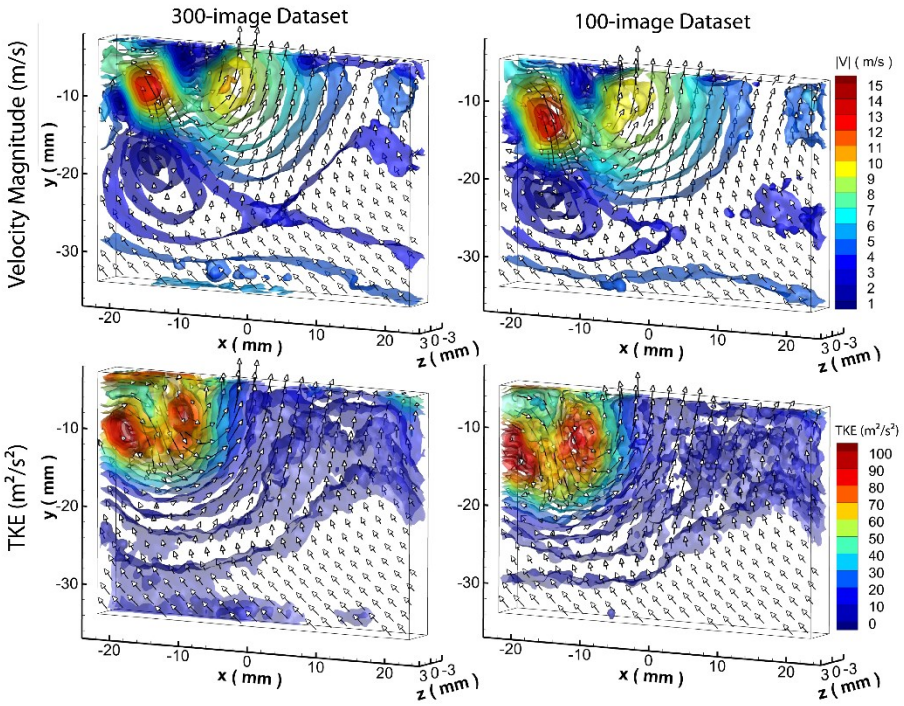

Supplemental figure caption: Comparison of 3D ensemble-average flow field and TKE for datasets containing 300 images (left) and 100 images (right). Local values are shown to change less than 5% (on average) as the sample size increases from 100 to 300. Each dataset shows consistent similarities such as (1) highest velocity magnitudes (15 m/s) occurring between the counter-rotating vortices and within the entrainment flow (10 m/s) and (2) regions of largest TKE are located near the center of the two counter-rotating vortices. Findings reveal that a 100-image sample size is suitable to study the relative flow changes as CAD progresses.

References

1. P.C. Miles, *Flow and combustion in reciprocating engines*, Springer-Verlag, Berlin Heidelberg, 2009, p. 173 (Chapter 4).
2. W. Zeng, M. Sjöberg, D.L. Reuss, *Int. J. Eng. Res*. (2014) 1-17.
3. R. Stiehl, J. Schorr, C. Krüger, A. Dreizler, B. Böhm, *Flow Turb. Combust.* 91 (3) (2013) 431-450
4. R. Stiehl, J. Bode, J. Schorr, C. Krüger, A. Dreizler, B. Böhm, *Int. J. Eng. Res.* (2016) doi: 10.1177/1468087416633541.
5. W. Zeng, M. Sjöberg, D.L. Reuss, *Proc. Combust. Inst.* 35 (2015) 2907-2914.

6. B. Peterson, D.L. Reuss, V. Sick, *Combust. Flame* 161 (2014) 240-255.
7. M. Zhang, M. Xu, D.L.S. Hung, *Meas. Sci. Technol.* 25 (2014).
8. B. Peterson, E. Baum, B. Böhm, V. Sick, A. Dreizler, *Proc. Combust. Inst.* 35 (2015) 2923-2931.
9. L.M. Itani, G. Bruneaux, L. Hermant, C. Schulz, *SAE Technical Paper* 2015-01-1902, 2015
10. S. Lind, L. Zigan, J. Trost, A. Leipertz, S. Will, *Int. J. Eng. Res.* (2015) 1-9.
11. J. Moreau, J. Boree, R. Brazile, G. Charnay, *Exp. Fluids* 37 (2004) 856-871.
12. N. Bharadwaj, C.J. Rutland, S. Chang, *Int. J. Eng. Res.* 10 (2009) 97-119.
13. S. Banerjee, C.J. Rutland, *SAE Technical Paper* 2012-01-0141, 2012.
14. S. Banerjee, C.J. Rutland, *Atomization and Sprays* 25(4) (2015) 285-316.
15. M. Sjöberg, W. Zeng, D. Reuss, *SAE Int. J. Engines* 7(2) (2014) 642-655.
16. W. Zeng, M. Sjöberg, D.L. Reuss, *SAE Int. J. Engines* 7 (2014) 615-632.
17. C. Disch, H. Kubach, U. Spicher, J. Pfeil, F. Altenschmidt, U. Schaupp, *SAE Technical Paper* 2013-01-0563, 2013.
18. Y.-J. Choo, B.-S. Kang, *KSME Int. J.* 17(7) (2003) 1095-1103.
19. E. Baum, B. Peterson, C. Surmann, D. Michaelis, B. Böhm, A. Driezler, *Proc. Combust. Inst.* 34 (2013) 2903-2910.
20. E. Baum, B. Peterson, B. Böhm, A. Dreizler, *Flow Turb. Combust.* 92 (1-2) (2014) 296-297.
21. F. Zentgraf, E. Baum, B. Böhm, A. Driezler, B. Peterson, *Phys. Fluids (1994-present)* 28(4) (2016) 045108.
22. K. Peterson, B. Regaard, S. Heinemann, V. Sick, *Optics Express* 20 (8) (2012) 9031-9037.
23. T. Van Overbrüggen, M. Klaas, B. Bahl, W. Schröder *SAE Int. J. Engines* 8(3) (2015) 1447-1461.
24. D. Freudenhammer, B. Peterson, C.-P. Ding, B. Boehm, S. Grundmann, *SAE Int. J. Engines* 8 (4) (2015) 1826-1836.
25. D.W. Green, R.H. Perry *Perry's Chemical Engineers' Handbook*, 8th edition., McGraw-Hill Inc., New York, 2008.

List of Figure Captions

Figure 1: Experimental setup.

Figure 2: PDF of $\Delta U/|V|_{3D,CV}$ (dash-lines, right/top axis) and HS-PIV/TPIV velocity differences (solid-lines, left/bottom axis).

Figure 3: Image sequence for instantaneous spray cycle. HS-PIV 78°-71°bTDC, TPIV (z=0mm) 70°bTDC.

Figure 4: Droplet response time vs. diameter.

Figure 5: 3D-TKE isosurfaces and ensemble-average velocity (100 cycles, every 29th vector shown, z=0mm) at select CADs.

Figure 6: 3D isosurfaces of instantaneous ||S|| (left), ||Ω|| (middle), and threshold-based ||Ω|| with 3C velocity field (z=0mm, every 21st vector shown) (right). Each CAD represents different cycles.

Figure 7: ||S||,||Ω|| PDFs of "spray-zone" at selected CADs. Non-injection PDFs represented at same CADs as injection.

Figure 8: (a-c) Average TKE, ||S||, and ||Ω|| isosurface density with CAD, (d-g) probability isosurfaces for ||Ω||≥12500s^{-1} at selected CADs.

Table 1: Engine operating conditions.

Table 1:
Engine operating conditions

Engine speed	800RPM
Intake press. / temp.	0.95bar / 300K
Fuel (C_8H_{18}) / EOI	2.9mg/cycle / 76°bTDC
Inj. Press. / Temp.	18MPa / 333K
Intake Press. / Temp	95kPa / 295K
Charge density at EOI	2.0 kg/m^3